



HAL
open science

Multiaxial loading on a 3D woven carbon fiber reinforced plastic composite using tensile-torsion tests: Identification of the first damage envelope and associated damage mechanisms

Nicolas Tableau, Zoheir Aboura, Kamel Khellil, Frederic Laurin, Julien Schneider

► To cite this version:

Nicolas Tableau, Zoheir Aboura, Kamel Khellil, Frederic Laurin, Julien Schneider. Multiaxial loading on a 3D woven carbon fiber reinforced plastic composite using tensile-torsion tests: Identification of the first damage envelope and associated damage mechanisms. *Composite Structures*, 2019, 227, pp.111305. 10.1016/j.compstruct.2019.111305 . hal-02632472

HAL Id: hal-02632472

<https://hal.science/hal-02632472>

Submitted on 27 May 2020

HAL is a multi-disciplinary open access archive for the deposit and dissemination of scientific research documents, whether they are published or not. The documents may come from teaching and research institutions in France or abroad, or from public or private research centers.

L'archive ouverte pluridisciplinaire **HAL**, est destinée au dépôt et à la diffusion de documents scientifiques de niveau recherche, publiés ou non, émanant des établissements d'enseignement et de recherche français ou étrangers, des laboratoires publics ou privés.

MULTIAXIAL LOADING ON A 3D WOVEN CARBON FIBER REINFORCED PLASTIC COMPOSITE, USING TENSILE- TORSION TESTS: IDENTIFICATION OF THE FIRST DAMAGE ENVELOPE AND ASSOCIATED DAMAGE MECHANISMS.

N. Tableau ^{a,b}, Z. Aboura ^b, K. Khellil ^b, F. Laurin ^c and J. Schneider ^a

^a Safran Aircraft Engines, Rond Point René Ravaud-Réau, 77550, Moissy Cramayel, France. Mail :
nicolas.tableau@safrangroup.com , julien.schneider@safrangroup.com

^b Laboratoire Roberval, UMR CNRS 7337, Université de Technologie de Compiègne, Centre de Recherche
Royallieu, 60203 Compiègne, France. Mail : nicolas.tableau@utc.fr, zoheir.aboura@utc.fr, kamel.khellil@utc.fr

^c ONERA (French Aerospace Lab), 29 Avenue de la Division Leclerc, 92320 Châtillon, France. Mail :
frederic.laurin@onera.fr

Abstract:

This study focuses on the experimental identification of the first damage envelope in a 3D woven composite with polymer matrix, under multi-axial loadings including combined in-plane tension and out-of-plane shear loadings (σ - τ envelopes). Proportional Tensile-Torsion tests on rectangular bars were performed to induce different multi-axial stress states. To enable envelopes identification, onset of the first damage has been evaluated thanks to the correlation of various and complementary investigation measurement techniques, such as Stereo-Digital Image Correlation (Stereo-DIC), Acoustic Emission (AE) and *in-situ* microscopic observations. In addition, a specific data reduction process has been used to manage accurate quantification of the stress state induced by the multi-axial loadings. Based on these findings, both σ_{11} - τ_{13} and σ_{22} - τ_{23} envelopes were identified on a 3D woven

composite material with polymer matrix. Using microscopic observations, damage mechanisms (type and localization) related to the multi-axial loadings were identified. In addition, thanks to the strain fields measured by the Stereo-DIC on the material surface, particular relations between the multi-axial loadings and the 3D woven architecture have been established.

KEYWORDS: 3D woven composite with polymer matrix, Multi-axial loading, first damage envelopes, damage mechanisms.

1. Introduction

Over the past years, tridimensional (3D) textile composites have been progressively used in many applications including aircraft, wind energy and more recently civil infrastructures [1]. Compared to the conventional 2D composite laminates, 3D woven composites provide many advantages. First, 3D woven structure permits to tailor the out-of-plane properties of the composite, to fulfill the requirement of particular applications. Furthermore, the tridimensional interlacing of the warp and weft yarns avoids the occurrence of large delamination cracks. As a result, 3D woven composites present higher damage tolerance and impact resistance than 2D composite laminates [2].

The introduction of 3D weaving architectures in composite materials induces totally different mechanical behavior and damage mechanisms, compared to classical 2D composite laminates [3]. Thus, most of knowledge that have been accumulated on the 2D composite laminates concerning characterization methods, mechanical behavior and damage mechanisms cannot be directly applied to 3D woven composites. As a consequence, a consistent effort is currently performed concerning the comprehension of the mechanical behavior and the damage mechanisms encountered in such 3D woven composites materials. Most of these studies concern uni-axial quasi-static [4-10], fatigue [11-12], and impact [13-14] loadings, but very

few works have been carried out on multi-axial loadings applied to 3D woven composites [15].

Thus, the first aim of this study is to identify the first damage envelope of a 3D woven composite in the case of multi-axial loadings, including combined in-plane tension and out-of-plane shear stress states. The second purpose of this study consists in giving a comprehensive analysis of the mechanical behavior of 3D woven composites, as well as the damage mechanisms induced by the considered multi-axial loadings. This particular stress state (especially its out-of-plane component) has been chosen because the considered 3D woven composites are very thick, and their out-of-plane behavior cannot be neglected in a context of structural part design. This work directly fits into this context by identifying relevant clues which can be used to validate numerical models.

Several tests have been developed by the scientific community to achieve a multi-axial state of stress in composite materials [16-17]. The most common test methods are (i) proportional axial tensile and torsion tests on tubular specimens [18], (ii) bi-axial tensile tests applied to the arms of a flat cruciform specimen [19] and (iii) Arcan tests [20]. Despite of the complexity concerning both specimen preparation and tests setting up, their application on composite materials has allowed identifying multi-axial combined in-plane tensile and in-plane shear stress failure envelopes. However, these tests are unable to provide simultaneously in-plane tension and out-of-plane shear stress states. In fact, very few tests are able to induce this specific multi-axial stress state. The most common test [21-22] consists in introducing simultaneously bending and torsion in a composite plate. Complex experimental device is required to introduce properly loadings, and extreme precautions have to be taken concerning the design of the grips to avoid any edge effect.

Thus, in this study, proportional tensile and torsion loadings on rectangular bars have been preferred to induce both in-plane tensile and out-of-plane shear stresses because of its relative

simplicity. Furthermore, single torsion induces pure and quasi-constant shear stress state on the overall faces and sides of the twisted bars, including the large Representative Unit Cell (RUC) of the 3D woven composite. However, extreme precautions have to be taken to master the induced multi-axial stress state.

This study is structured in 6 main parts: In section 2, the material is briefly described. In section 3, experimental conditions are discussed: the geometry of the sample, as well as the investigation measurement techniques, and the testing protocol are explained. In section 4, the method to quantify with a great accuracy the stress levels related to multi-axial loading is explained. The experimental method used to determine the damage onset, thanks to the multi-instrumented methodology, is also described. In section 5, the first damage envelope of the 3D woven composite material is given. In addition, damage mechanisms as well as their relations with the multi-axial loading and the 3D woven architecture are discussed.

2. Material

The material under investigation includes intermediate modulus (IM) carbon fibers woven into a tridimensional Interlock preform associated with an epoxy resin. This composite material, provided by Safran group, is obtained by Resin Transfert Molding (RTM). Dimensions of the 3D woven preform along the warp yarns direction (axis 1 on Figure 1), the weft yarns direction (axis 2), and through-the-thickness (axis 3) are included between 20 and 40 mm and yarns sections are of millimeter size. It is worth mentioning that its RUC is rather large as compared to other 2D woven composites. Moreover, it can be noticed that this material is highly unbalanced, due to the different volume ratios between weft and warp yarns.

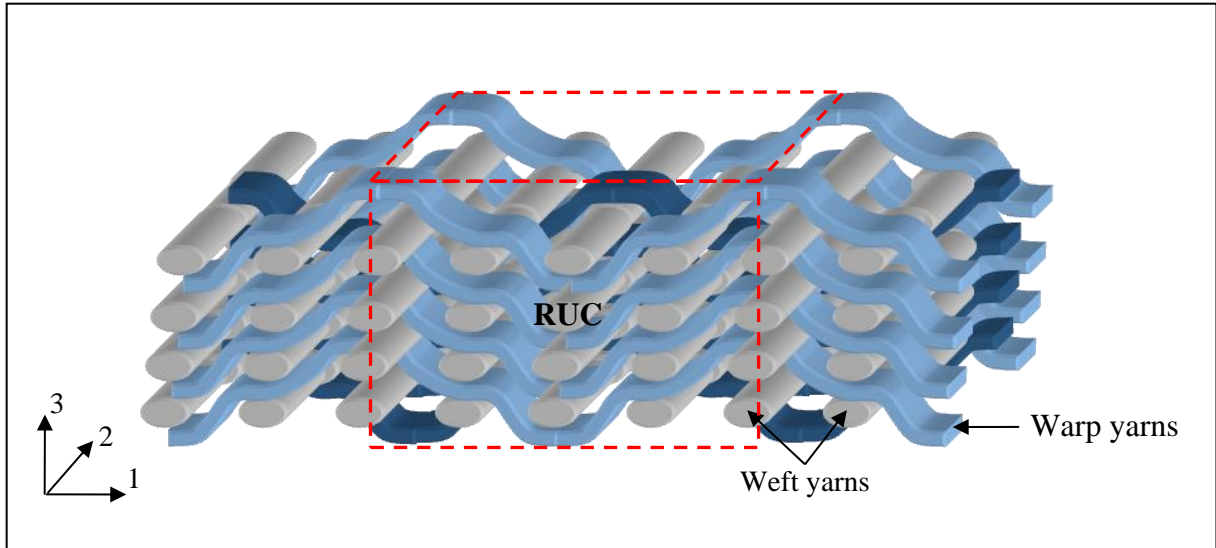


Figure 1 : Illustration of a typical woven pattern included in a 3D woven Composite.

3. Experimental conditions

3.1. Sample geometries

The aim of this experimental study consists in determining experimentally the first damage envelope of a 3D woven composite material with polymer matrix for different multi-axial stress states including both in-plane tensile and out-of-plane shear stresses. Thus, the other type of stresses induced by proportional tensile-torsion loading on rectangular bars must be negligible.

Tensile loading F induces a constant stress σ_{xx} over the entire section of a bar defined by its length denoted L , its width denoted b and its thickness denoted h (following respectively x , y , z axis as seen on Figure 2). The relation between F and σ_{xx} is given below:

$$\sigma_{xx} = \frac{F}{bh} \quad (1)$$

It is well known that tensile loading performed on a rectangular bar induces tensile stress concentration close to the the sample fixtures. To decrease this stress concentration level, samples have been bonded with 45° tapered aluminum tabs.

Torsion induces both shear stresses on face and sides of the bar. Assuming at least homogeneous and orthotropic behavior of the material, Lekhnitskii's theory [23] can be used to evaluate shear stresses on both faces and sides of the bar. These relations are given below:

$$\tau_{xy} = \frac{M}{bh^2} k_1 \quad (2.1)$$

$$\tau_{xz} = \frac{M}{bh^2} \sqrt{\frac{G_{xz}}{G_{xy}}} k_2 \quad (2.2)$$

$$\text{where } k_1 = \frac{8c}{\pi^2 \beta(c)} \sum_{n=1,3,5,\dots}^{\infty} \frac{(-1)^{(n-1)/2}}{n^2} \tanh \frac{n\pi}{2c} \quad (2.3)$$

$$\text{and } k_2 = \frac{c}{\beta(c)} \left(1 - \frac{8}{\pi^2} \sum_{n=1,3,5,\dots}^{\infty} \frac{1}{n^2 \cosh \frac{n\pi}{2c}} \right) \quad (2.4)$$

$$\text{with } \beta(c) = \frac{32c^2}{\pi^4} \sum_{n=1,3,5,\dots}^{\infty} \frac{1}{n^4} \left(1 - \frac{2c}{n\pi} \tanh \frac{n\pi}{2c} \right) \quad (2.5)$$

$$\text{and } c = \frac{b}{h} \sqrt{\frac{G_{xz}}{G_{xy}}} \quad (2.6)$$

where M is the applied torque. τ_{xy} and τ_{xz} are the maximum shear stresses induced respectively on the faces and sides of the bar. G_{xy} and G_{xz} are respectively shear modulus in the (x,y) and (x,z) plans of the material.

k_1 and k_2 are both St Venant's coefficients. Their values strongly depend on the bar geometry, and in a minor way, on the material shear rigidities. To magnify k_1 and minimize k_2 values, bar width b must be significantly higher than its thickness h . This condition ensures higher

level of maximum shear stress (τ_{xy}) on the upper and lowest bar faces and a lower level of maximum shear stress (τ_{xz}) on its sides. As a consequence, this geometrical configuration ($b \gg h$) ensures the simultaneous emergence of the first damages on the upper and lowest bar faces and avoids parasitical damages on its sides.

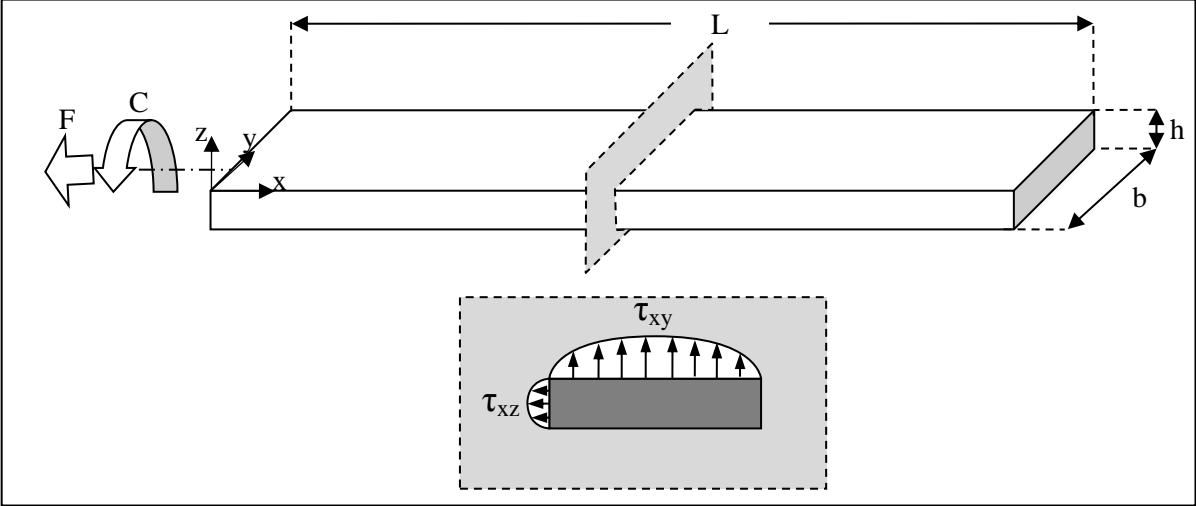


Figure 2 : Illustration of typical sample geometry and related shear stresses induced by torsion.

In the case of this study, out-of-plane shear stress value should be magnified, and in-plane shear stress value must be decreased as much as possible. To ensure this objective, all samples were extracted from a thick 3D woven composite plate following the scheme illustrated on Figure 3 :

- One first set of 5 rectangular bars were collected following the warp direction (along the axis 1). This set has been used to magnify σ_{11} - τ_{13} multi-axial stress states on upper and lowest bar faces (where σ_{11} is the tensile stress value following the axis 1 and τ_{13} is the shear stress value in plane 1-3).
- A second set of 4 bars has been collected following the weft direction (along the axis 2). This second set, which has the same dimensions as the first one, has been used to

induce σ_{22} - τ_{23} multi-axial stress states on upper and lowest bar faces (where σ_{22} is the tensile stress value following the axis 2 and τ_{13} is the shear stress value in plane 2-3).

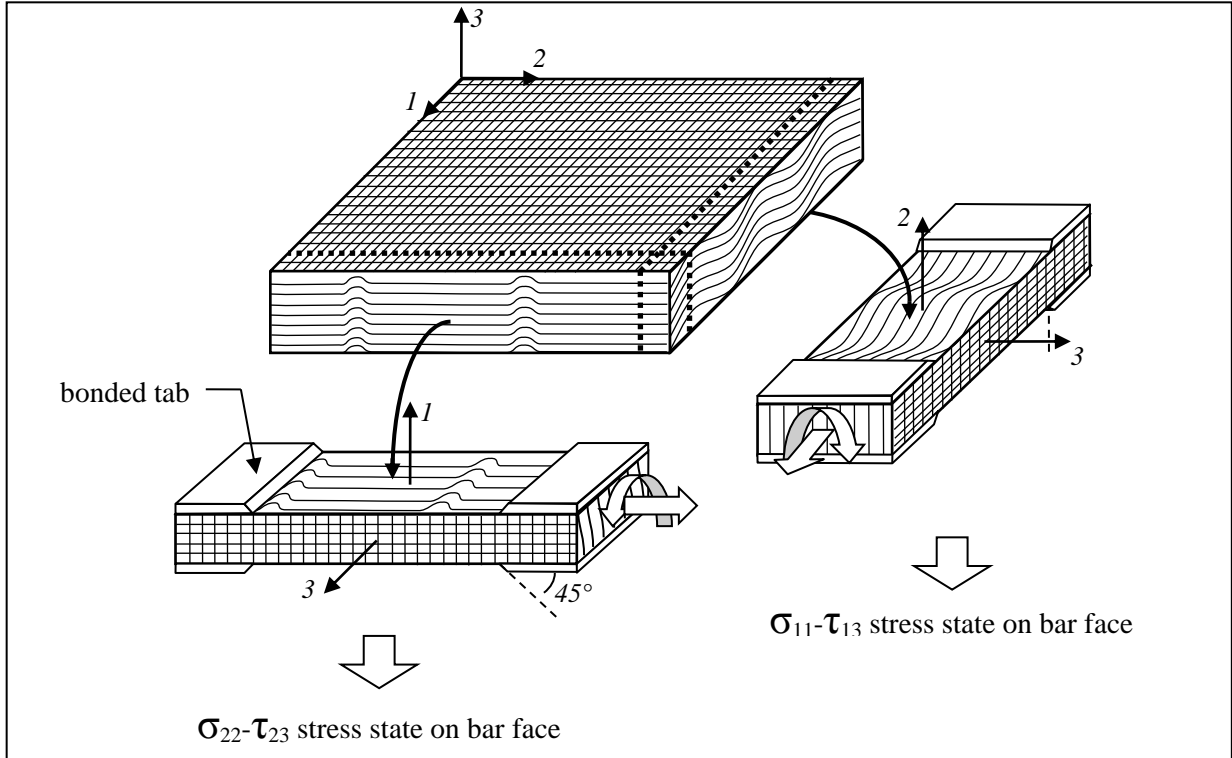


Figure 3 : Typical sampling scheme of the samples collected in a thick 3D woven composite plate.

3.2. Investigation measurement techniques

Proportional tensile-torsion tests on rectangular bars have been fully multi-instrumented. Stereo-DIC, as well as Acoustic Emission (AE) acquisition and *in-situ* video-microscopy have been used simultaneously during each test. To achieve this multi-instrumented approach, samples have been prepared carefully as shown in Figure 4. During tests, all investigation measurement techniques have been set up on the axial-torsional test system as illustrated in Figure 5. Typical sample preparation and setting up details are given below:

- Stereo-DIC system has been set up in front of the samples front face. This system has been used to measure tridimensional position, displacement and strain fields on a restrained area covering the entire width of the samples and extending from 30% to

70% of the sample length. The length of this observation area has been fixed to avoid the edge effects and their consequences on the shear modulus identification [23]. To facilitate the correlation process, an artificial grey-level speckle has been painted on this observation area, as shown in Figure 4. Pictures acquisition and stereo correlation have been performed using the commercial ARAMIS system (provided by Gom[®]). Each camera (Model 5M) includes a square sensor of 2448*2048 px² and a 50mm lens (Model Titanar). Regarding the spatial resolution of the grey-level speckle, the Zone Of Interest (ZOI) has been fixed to 30*30 px² for the correlation process.

- Acoustic Emission (AE) acquisition has been used to record potential material acoustic activity during loadings. Two AE sensors (Model micro80 provided by Mistras[®]) have been clamped on samples back face to enclose the Stereo-DIC observation area. The simultaneous use of these two sensors allows localizing source of each acquired signal. Using this localization process, signals coming away from the area of interest covered by the two AE sensors have been removed. AE acquisition and post processing have been both performed using the commercial AEWIn software, provided by Mistras[®].
- In-situ video microscopy has been focused on the back face of the samples, on a polished area located at the middle of the restrained area. *In-situ* taken pictures have allowed localizing the onset of damages on lower surface and their development in the 3D woven composite, during each test. Regarding the wide range of the potential damaged area, cartographies have been assembled from several taken pictures, both to ensure a sufficient resolution to detect early damages and to cover a large area, representative of the 3D woven composite mesoscale (*i.e.* covering at least one material RUC along the longitudinal direction of the bar).

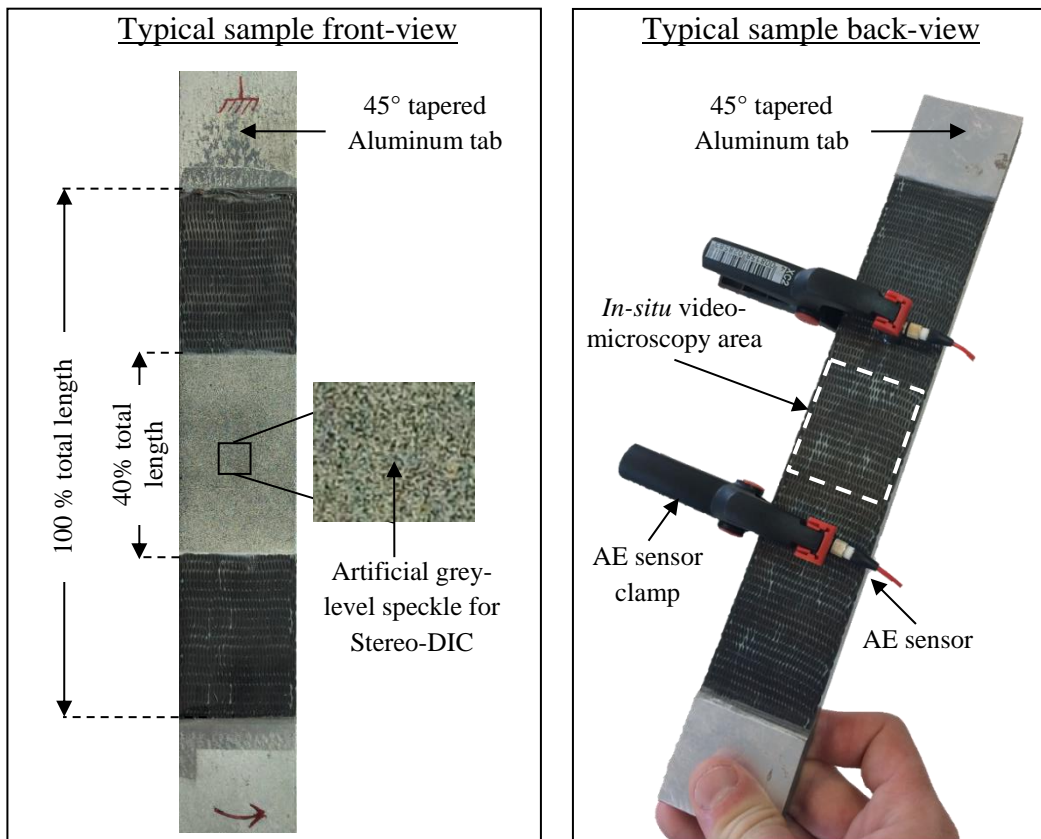


Figure 4 : Typical sample preparation to perform tensile-torsion tests.

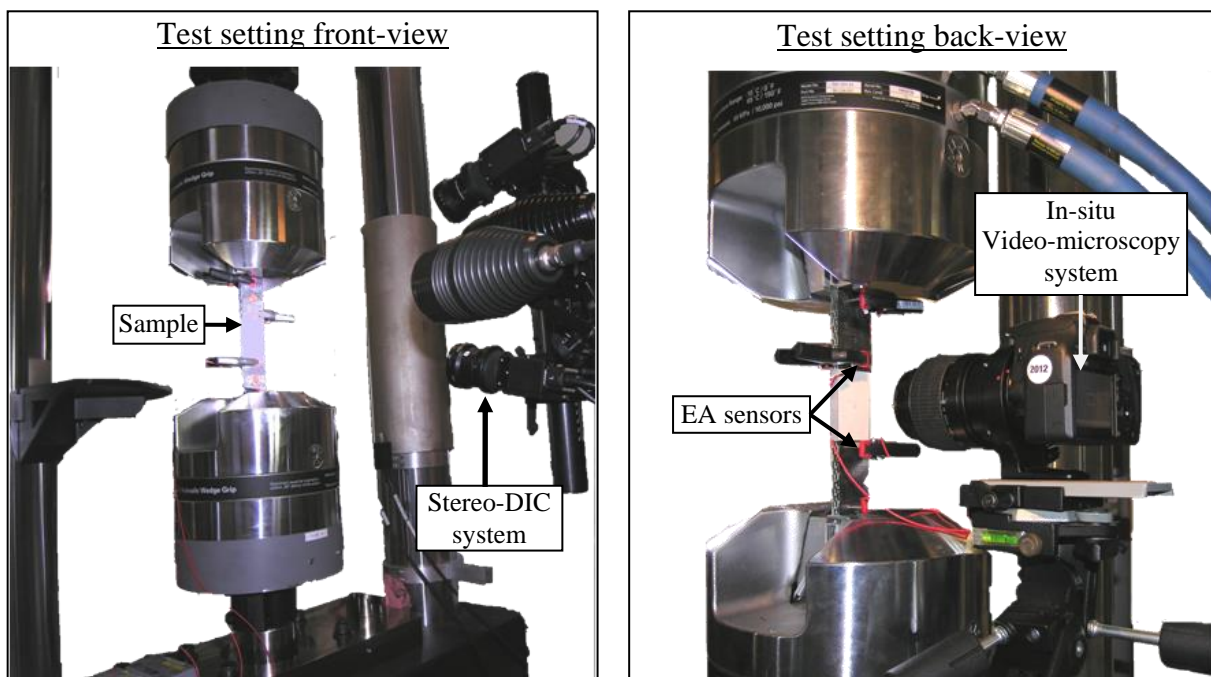


Figure 5 : Illustration of the investigation measurement techniques setting up during tensile-torsion tests.

3.3. Testing protocol

To identify onset and development of damages, a specific testing protocol has been applied to the tested samples. This protocol, summarized in Figure 6, includes a succession of incremental multi-axial loadings (including simultaneously tensile and torsion loadings), to progressively increase multi-axial tensile and shear stress quantities in the material. Typically, a large first step is applied to quickly reach a stress level just close but lower than the potential damage level. Then, the following incremental steps are fixed closer one to each other (step $\approx 10\text{MPa}$) to ensure the accurate measurement of the stress level giving the damage onset.

Before and after each incremental multi-axial loading, individual tensile (F) and torsion (M) loadings are applied successively to the sample, to evaluate the initial and then the residual tensile modulus as well as the initial and the residual out-of-plane shear modulus. These complementary uni-axial loadings were provided at a constant level, low enough to ensure no damage onset or propagation. Concerning torsion, this low level has also allows attenuating viscous effects during the shear modulus measurement.

After each incremental step, cartographies are taken by the means of the *in-situ* video-microscopy system, to detect and localize the onset of damages.

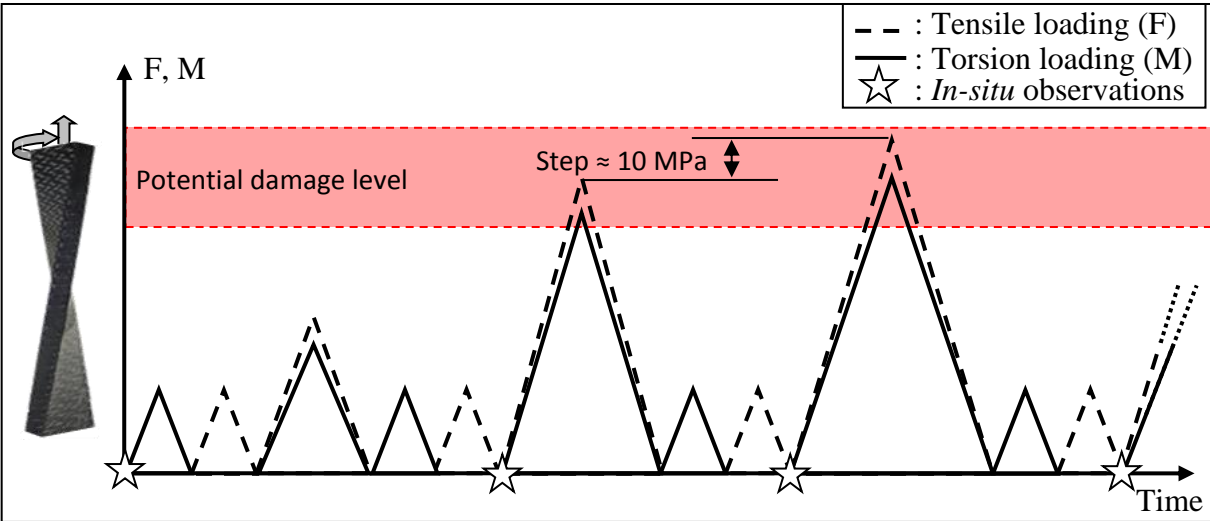


Figure 6 : Illustration of typical testing protocol during multi-axial tensile-torsion tests.

During each uni-axial loading, tensile modulus (E_{xx}) and shear modulus (G_{xy}) are identified following the methods explained below:

- Macroscopic tensile modulus (E_{xx}) is evaluated using Hooke's relation ($E_{xx} = \sigma_{xx} / \epsilon_{xx}$) where the longitudinal stress (σ_{xx}) is directly deduced from the tensile load applied during the test ($\sigma_{xx} = F / (bh)$) where b and h are directly measured on the samples before the test) and the averaged value of the longitudinal strain field (ϵ_{xx}) measured by stereo-DIC on the observed area.
- Macroscopic shear modulus (G_{xy}) is measured by the means of the Lekhnitskii's relation given below (eq. 3). To avoid any edge effect during experimental measurement of the shear modulus, the twist angle per unit length (θL) is directly deduced from the tridimensional position and the displacement fields, measured by Stereo-DIC on the restrained area, using specific geometrical transformations [24].

$$G_{xy} = \frac{ML}{\theta bh^3 \beta(c)} \quad (3)$$

where M is the applied torque and θ is the twist angle of the tested bar. To manage the calculation of the function $\beta(c)$ the infinite sum is approached using index i in a range of values between 1 and 99.

To evaluate accurately the macroscopic shear modulus G_{xy} , as well as the shear stress quantity at the upper and lower bar faces τ_{xy} , simultaneous intervention of both G_{xy} and G_{xz} shear modulus, occurring into the warping function $\beta(c)$, must be managed. To do so, most of experimenters [24-25] assume the isotropic behavior of the material (meaning $G_{xz} / G_{xy} = 1$). It can be considered surprising to consider this ratio equal to 1 for the studied orthotropic

material. Nevertheless, it can be noticed that bars have their width b significantly higher than their thicknesses h ($b/h = 4$). Considering the evolution of the warping function $\beta(c)$ (Figure 7), which is strongly dependant of the dimensions ratio (b/h) and in a minor way of the ratio G_{xz}/G_{xy} (due to the presence of the square root), we can assume the fact that $\beta(c)$ reaches almost its asymptotic value in the case of our sample's geometry. As a consequence, the ratio G_{xz}/G_{xy} has been fixed to 1 in the term $\beta(c)$ for the rest of the study. In order to validate *a posteriori* this assumption, initial out-of-plane shear modulus measured during these tests have been compared with those measured by the mean of Iosipescu and three points bending tests [9]. This comparison revealed at most 10 % gap between both methods (Table 1). This comparison demonstrates the relevance of the ratio ($b/h = 4$) for the shear modulus identification, as well as for the shear stress level identification.

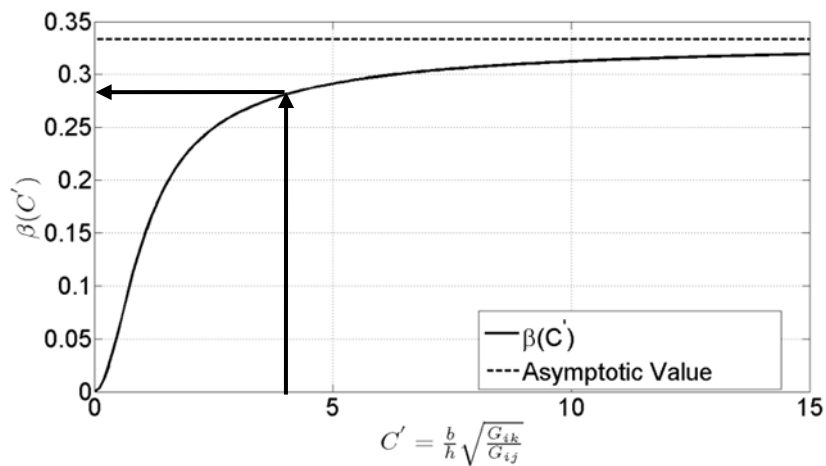


Figure 7 : Evolution of the warping fonction $\beta(c)$.

	torsion tests (Reference)	Iosipescu tests	Three points bending tests [9]
G_{13} (Dimensionless)	1	1,06	1,1
G_{23} (Dimensionless)	1	0,98	0,92

Table 1 : Comparison between shear modulus measured by the means of torsion, Iosipescu, and three points bending tests [9] (each modulus has been rationed by torsion test value, taken as a reference).

All the tensile-torsion tests have been performed using an axial-torsional testing system (Model 809 provided by MTS[®]) equipped with hydraulic wedge grips (Model 647 provided by MTS[®]). Tests have been controlled simultaneously by torque and axial load rates. Torque rate has been fixed at a constant value for all tests (2° per minute) to ensure that viscous effects were almost low and identical. Axial load rates have been then adapted to reach different fixed stress ratios (σ_{xx}/τ_{xy}) during multi-axial loadings.

4. Test method analysis

4.1. Shear stress state evaluation under multi-axial loadings

To generate damages (onset and development), relatively high shear stress levels have to be applied to the composite material. Thus, elevated twist angles must be applied on the rectangular bar, inducing notable modifications on the bar face stress state. In their work, Gong & al. [27] demonstrated that these variations of the stress state were directly linked to the modification of the initial bar length (L). The relation given below has been developed by the authors to link the twist angle (θ) and the modified bar length (L') in its swiveled position, as illustrated in Figure 8:

$$L' = \frac{b\theta}{2} \frac{1}{\sinh\left(\frac{b\theta}{2L}\right)} \quad (4)$$

In the case of proportional tensile and torsion loadings, this modified length (L') is magnified by the adding of the axial tensile load (F). In this particular case, the modified length (L') becomes:

$$L' = \frac{b\theta}{2} \frac{1}{\sinh\left(\frac{b\theta}{2L}\right)} + \frac{FL}{bhE_{xx}} \quad (5)$$

The modification of this initial bar length induces a contrary twisting moment which attenuates the shear stress level. Only a part of the applied torque (M) does effectively induce

shear stresses on the bar faces (τ_{xy}) and sides (τ_{xz}). This effective torque (M_{eff}) can be estimated using the relation:

$$M_{\text{eff}} = M - \frac{\frac{b\theta}{3L} - \sqrt{1 + \left(\frac{1}{\varphi}\right)^2} + \left(\frac{1}{\varphi}\right)^2 \ln(\varphi + \sqrt{1 + \varphi^2})}{A} \quad (6.1)$$

$$\text{where } \varphi = \frac{b\theta}{2L'} \quad (6.2)$$

$$\text{and } A = \frac{4}{E_{xx}hb^2} \quad (6.3)$$

Then, by combining the relations given by Lekhnitskii [23] and Gong & al. [27], tensile effective stress ($\sigma_{xx \text{ eff}}$) and shear effective stress ($\tau_{xy \text{ eff}}$) occurring on upper and lower bar faces follow the relations:

$$\tau_{xy \text{ eff}} = \frac{M_{\text{eff}}}{bh^2} k_1 \quad (7)$$

$$\sigma_{xx \text{ eff}} = \frac{E_{xx}}{L} \int_{-b/2}^{b/2} \left(\sqrt{\left(\frac{bh}{2\varphi}\right)^2 + \theta^2 y^2} - L \right) dy \quad (8)$$

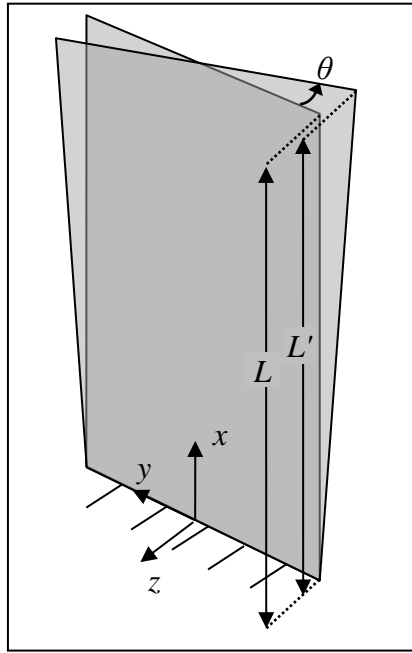


Figure 8 : Illustration of the deformation of the rectangular bar under high torsion level.

To evaluate the relevance of these analytical stress corrections, simulations have been made using a Finite Element Model (FEM) representative of the investigated bars. All calculations have been performed with the commercial code ABAQUS/standard, using an implicit solver, relevant for quasi-static tests. A representative mesh of bars used for calculation is illustrated in Figure 9. Meshes have been refined near the fixtures where the boundary conditions are applied. Local refinement of the mesh has also been processed through the section of the bars (smallest elements near the surfaces) to describe as best as possible the theoretical evolution of the shear stresses through the thickness and through the width of the bars. Twenty-node quadratic brick elements with reduced integration (so-called C3D20R elements) have been chosen. A fixed boundary condition has been applied to the surface nodes on one side of the bars. On the other side, surface nodes have been linked to a master node. Torque (M) around the axis 1 and axial tensile load (F) have been then applied on this master node, to ensure both tensile stress (σ_{11}) and shear stress ($\tau_{13} = \sigma_{11}/3$) quantities. The behavior of the studied 3D woven composite material is assumed to be orthotropic linear elastic, while that of the aluminum tabs is assumed isotropic linear elastic. All simulations have been performed

considering geometrical non linearity (using Jaumann rate formulation). Shear and tensile stress levels ($\sigma_{11 \text{ FEM}}, \tau_{13 \text{ FEM}}$), as well as strains ($\epsilon_{11 \text{ FEM}}, \epsilon_{13 \text{ FEM}}$) have been estimated in a restrained area (40% of the total bar length between fixtures) to avoid any edge effect.

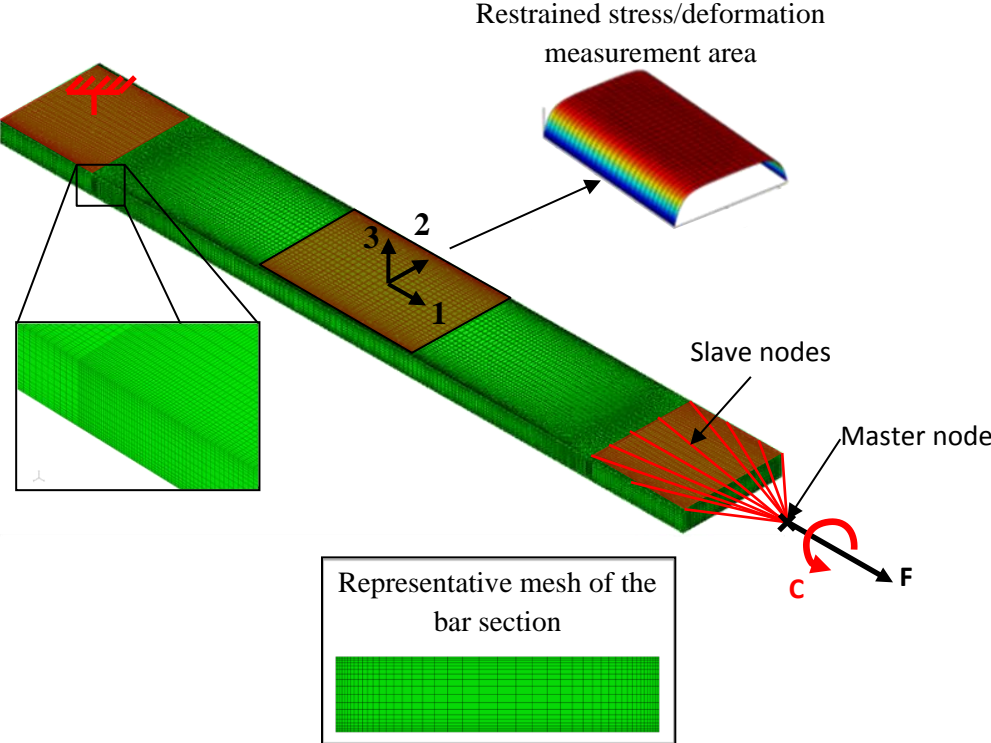


Figure 9 : Illustration of the FEM used to perform proportional tensile – torsion simulations.

Tensile and shear stress evolutions estimated with the FEM simulation are provided in Figure 10 (blue dashed line). As a comparison, levels of stress obtained with analytical approaches (considering the same levels of torque and tensile loads introduced in the FEM) are also given. The black dashed lines represents stress levels given by the simple application of Lekhnitskii’s theory (eq. 1 and eq. 2.1) while the red dashed lines represent effective stress levels (eq. 7 and eq. 8). As illustrated in this figure, levels of stress estimated with direct application of Lekhnitskii’s theory markedly overestimate the shear stress level and in a least significant way the tensile stress level given by FEM simulations, considered as the reference. On the contrary, the effective stress levels, after correction, are nearly the same than those

estimated with FEM. Thus, these results demonstrate the relevance of the analytical stress corrections.

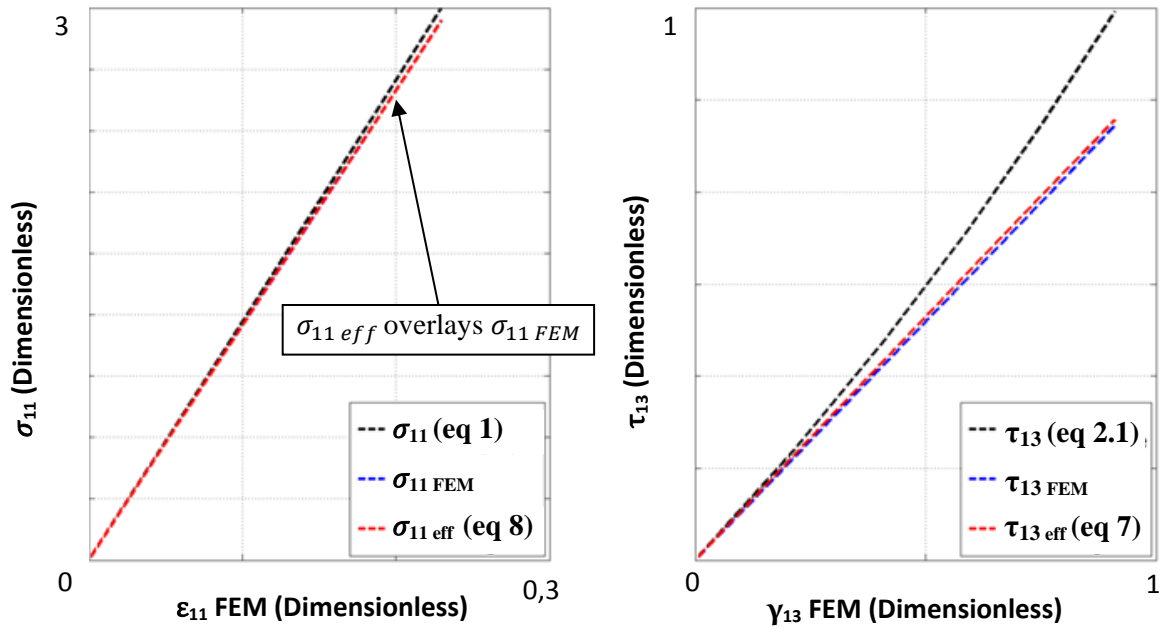


Figure 10 : Comparison between stress levels issued from analytical relations and FEM measurement.

To manage both estimation of tensile and shear modulus, as well as shear and tensile stresses, an automatic data processing algorithm has been developed using the commercial software Matlab[®]. Input data such as load and torque levels (F,M) were directly given by the axial/torsional testing system. Twist angle (θ) has been deduced using geometrical transformations [24], from the tridimensional position and displacement fields measured by the Stereo-DIC on the 40% bar length restrained area.

4.2. Damage onset identification

Damage onset is identified by correlating complementary results given by each investigation tool (material mechanical response, acoustic activity and *in-situ* micrographs). Figure 11 illustrates an example of multi-axial incremental loadings that have been performed on one sample subjected to a fixed stress ratio ($\sigma/\tau = 3$). This test includes a total of 6 incremental multi-axial loadings. After the third one, the residual shear modulus starts decreasing, which

indicates a potential damage onset on the material. Simultaneously, notable acoustic activity is recorded, which confirms the fact that major damage mechanisms begins to occur. At the same time, *in-situ* observations allow to determining the type of damage mechanisms and first matrix cracks are detected. Based on these complementary measurements, first damage onset can be set at the maximum shear and tensile stress quantities that have been reached during the second multi-axial loading, in order to provide conservative values. Above these stress levels, the simultaneous occurrence of three main damage indicators (macroscopic shear rigidity loss, acoustic activity and observation of major damage mechanisms) confirms robustly the development of damages.

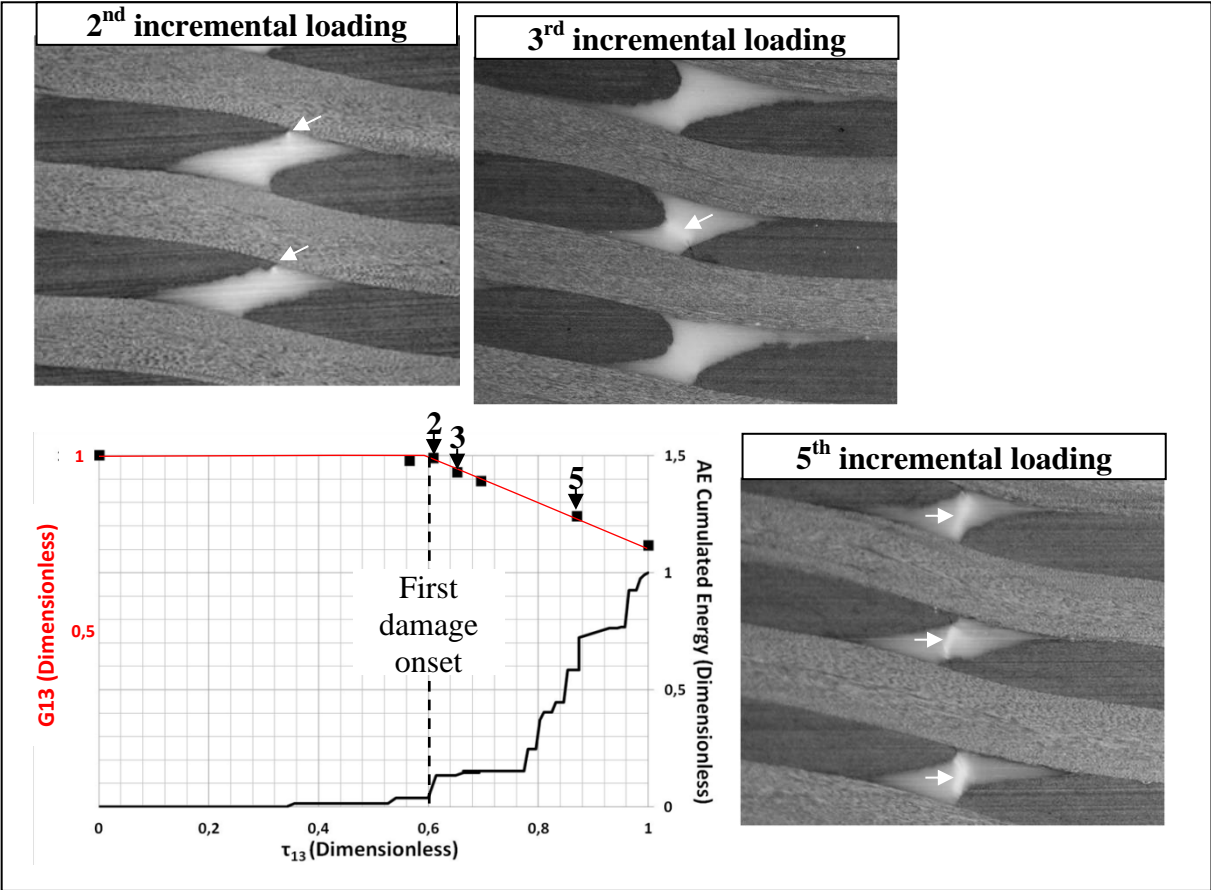


Figure 11 : Typical cross-data used to identify damage onset and damage evolution under multi-axial tensile-torsion loading.

5. Results and discussion

5.1. First damage envelopes and associated damage mechanisms : plan $\sigma_{11} - \tau_{13}$

First set of 5 bars, collected following the warp yarns direction, has been tested using different stress ratios (σ_{11} / τ_{13}) to cover a large part of the multi-axial first damage envelope in the stress plan ($\sigma_{11} - \tau_{13}$).

A typical stress-strain curve issued from one of these multi-axial tests is illustrated on Figure 12. The $\gamma_{13} - \tau_{13}$ curve shows that a viscous component affects the out-of-plane shear behavior of the composite, even before the first damage onset (black cross on the figure) while any significant viscous component is visible on the $\epsilon_{11} - \sigma_{11}$ curve. Each uni-axial shear loading intermediate step shows a linear behavior without any hysteresis, as reported in Figure 12, allowing measuring accurately the evolution of the out-of-plane shear modulus during the loading without spurious assumption.

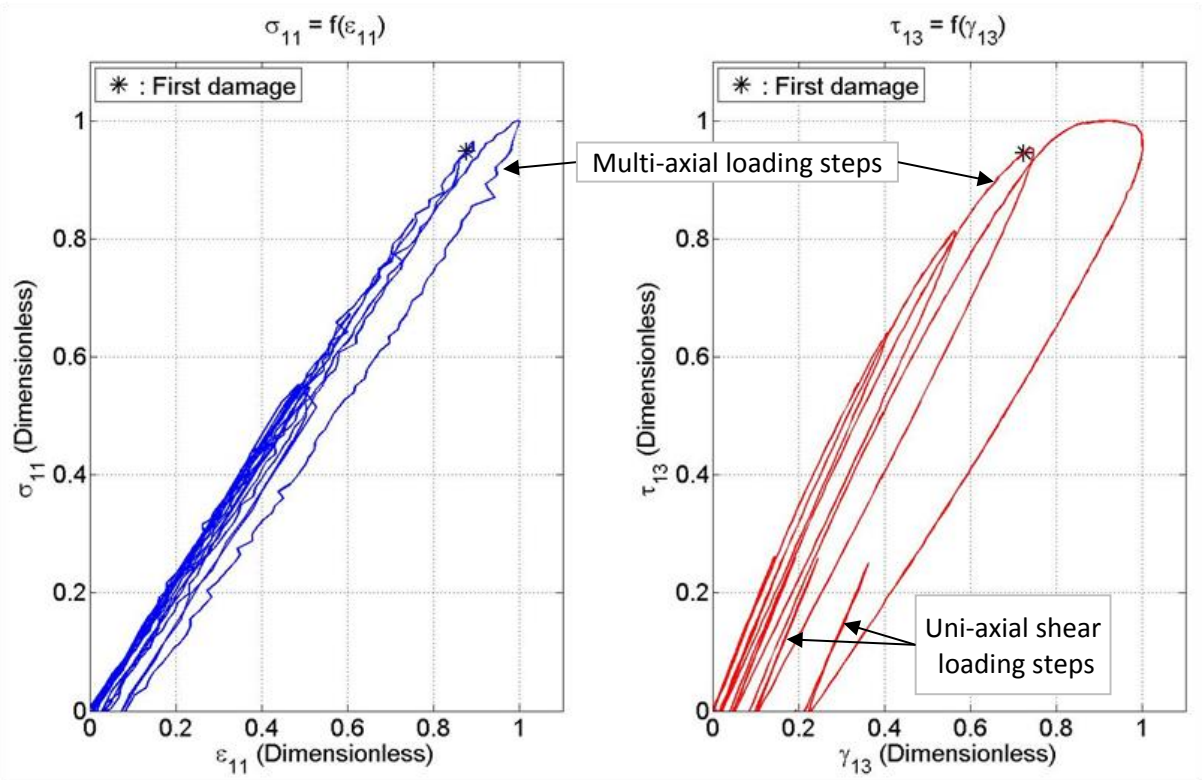


Figure 12 : Typical Stress-strain curve issued from multi-axial loading tests.

Damage envelope issued from all the tests is illustrated on Figure 13. Damage mechanisms induced by specific loading conditions (tensile, torsion and proportional tensile-torsion loading) are also illustrated. From the observed damage mechanisms, several remarks can be set:

- In the case of tensile loading (case 1), most of damage mechanisms are matrix cracks, oriented at $+45^\circ$ (respectively at -45°) localized on descents (respectively on climbs) of the warp yarns path.
- In the case of torsion loading (case 2), most of damage mechanisms are debondings between warp and weft yarns. These mechanisms occur on the overall RUC, including climbs, descents, tops and bottoms of the warp yarns path.
- In the case of proportional tensile-torsion loading (case 3), damage mechanisms consist in a combination of both matrix cracks and debondings between weft and warp yarns. Unlike damages induced separately by tensile and torsion loading, damage mechanisms only occur on the descent of the warp yarns path. Other areas are not damaged.

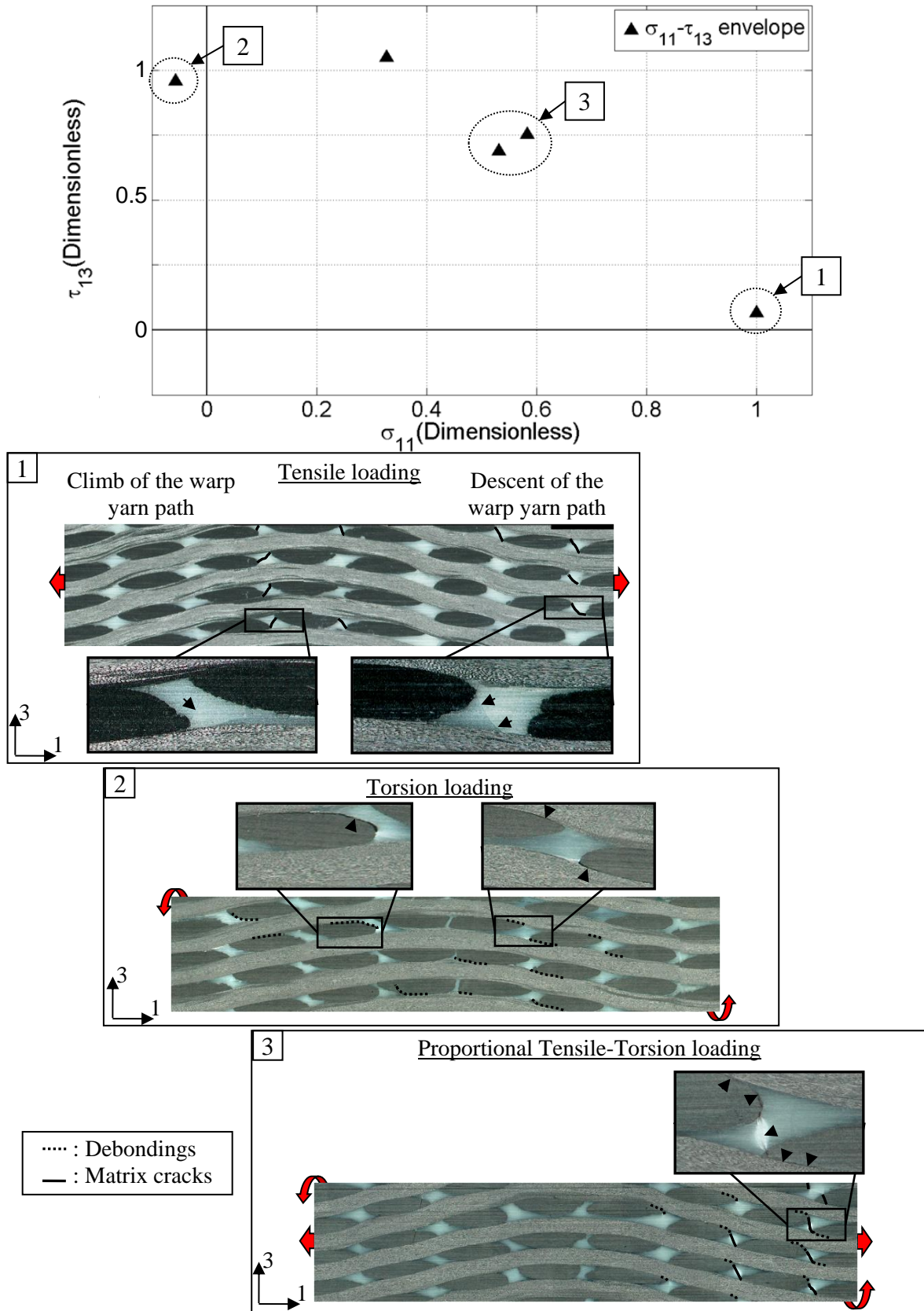


Figure 13 : First damage envelope on the $\sigma_{11} - \tau_{13}$ plan and illustration of the typical damage mechanisms observed under tensile (1), torsion (2) and proportional tensile-torsion (3) loadings.

To understand the relations that link each loading to the damage characteristics (type and location), longitudinal (ϵ_{11}) and shear strain fields (γ_{13}) measured by Stereo-DIC have been illustrated in the case of an uni-axial tensile loading (first row on Figure 14), in the case of simple torsion loading (second row), and in the case of proportional tensile-torsion loading (third row). To be able to compare quantitatively strains evolution along the warp yarns direction for each type of loading, virtual gauges have been applied on each strain field (black solid line superimposed to each strain fields). Each value of these virtual gauges cover the entire width of the bars (i.e. the whole thickness of the 3D woven composite) and one of each successive data point of the strain field grid, following the warp yarns direction. Finally, the warp yarn path is described on the top of each strain field (black dotted line) to be able to compare strain evolution with the 3D woven architecture.

As seen on Figure 14, all the strain fields clearly show a succession of identical sequences following the warp direction. The offset between each repeated sequences corresponds exactly to the composite's RUC. Each type of loading induces different strain field patterns:

- Tensile loading induces a quasi-constant longitudinal strain (ϵ_{11}) along warp yarns direction. In addition, a periodic shear strain component appears (γ_{13}). This additional component can be directly linked to the undulated arrangement of the warp yarns which tend to realign in the load direction during tensile loading, inducing alternatively up and down movements of weft yarns columns (Figure 15). These relative movements induce local shear strain between each weft yarns columns. Across one entire composite RUC, this shear strain component is successively negative on climbs and positive on descents of the warp yarns path. This shear

component could explain the numerous matrix cracks oriented at $+45^\circ$ on climbs and at -45° on descents of the warp yarns path (Figure 13).

- Torsion loading induces a quasi-constant shear strain, as well as a periodic longitudinal strain component (compression on climbs and tension on descents of the warp yarns path). It can be noted that shear strain level is much more important than in the case of tensile loading. This higher strain component seems to be linked to the numerous debondings illustrated in Figure 13. The sliding between the warp yarns during torsion could explain these specific damage mechanisms.
- Proportional tensile-torsion induces strain fields that are nearly equivalent to the sum of those individually induced by tensile and torsion loadings. Consequently, periodic longitudinal strains induced by torsion decrease on climbs and increase on descents of the warp yarns path the quasi-constant longitudinal strain induced by tensile loading. Thus, higher longitudinal strain level appears on descents whereas attenuate ones appear on climbs. Concerning the shear strain fields, the same phenomenon is occurring. As a result, descents of the warp yarns path are strongly charged while climbs are relieved. This summation of the strain fields explains the fact that only the areas included in the descent of the warp yarns path are damaged. It also could explain the fact that both matrix cracks and debondings occur in the case of proportional tensile torsion loading (Figure 13).

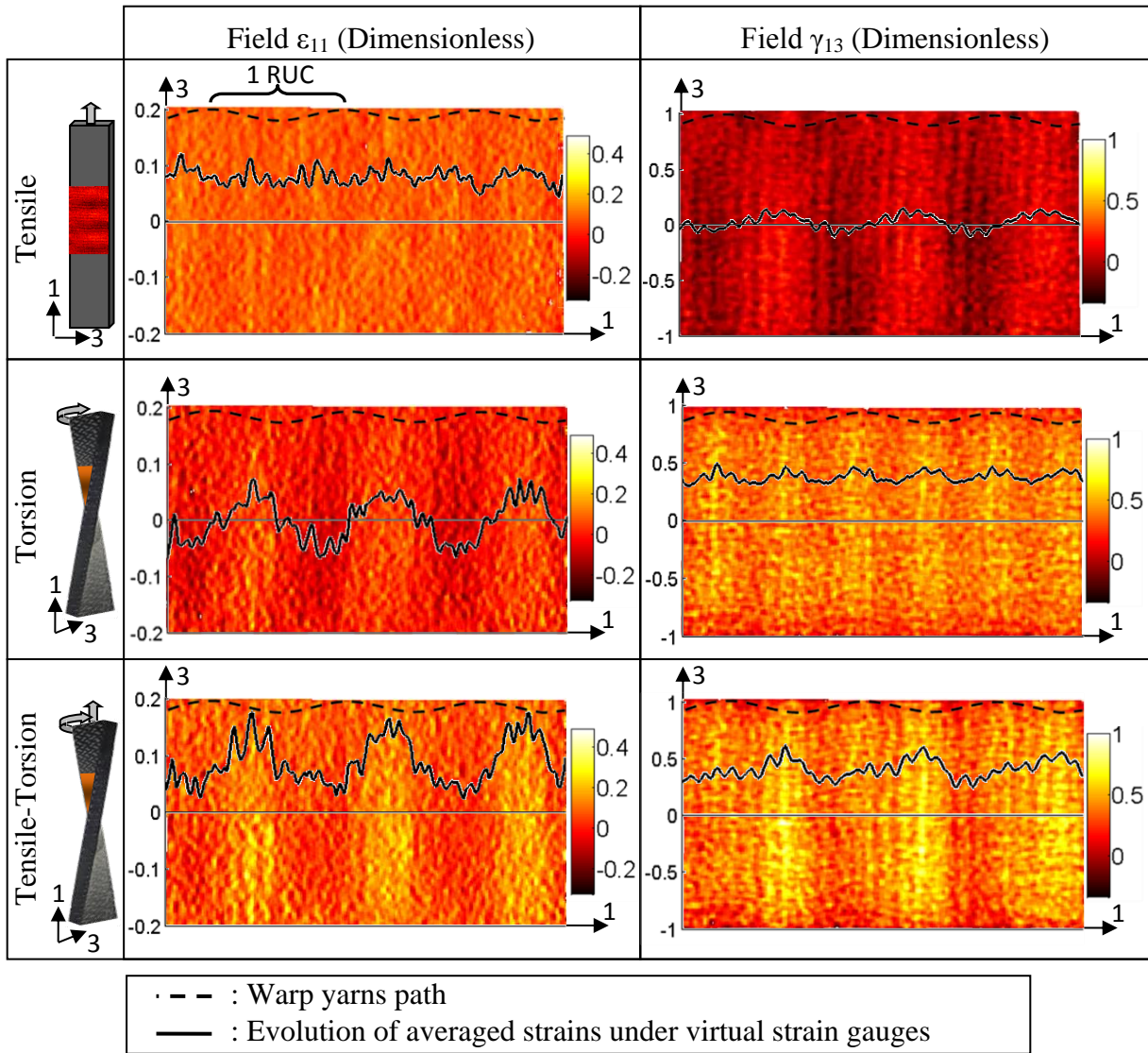


Figure 14 : Illustration of the strain fields ϵ_{11} and γ_{13} measured by Stereo-DIC on the bar face during tensile, torsion and proportional tensile-torsion loadings.

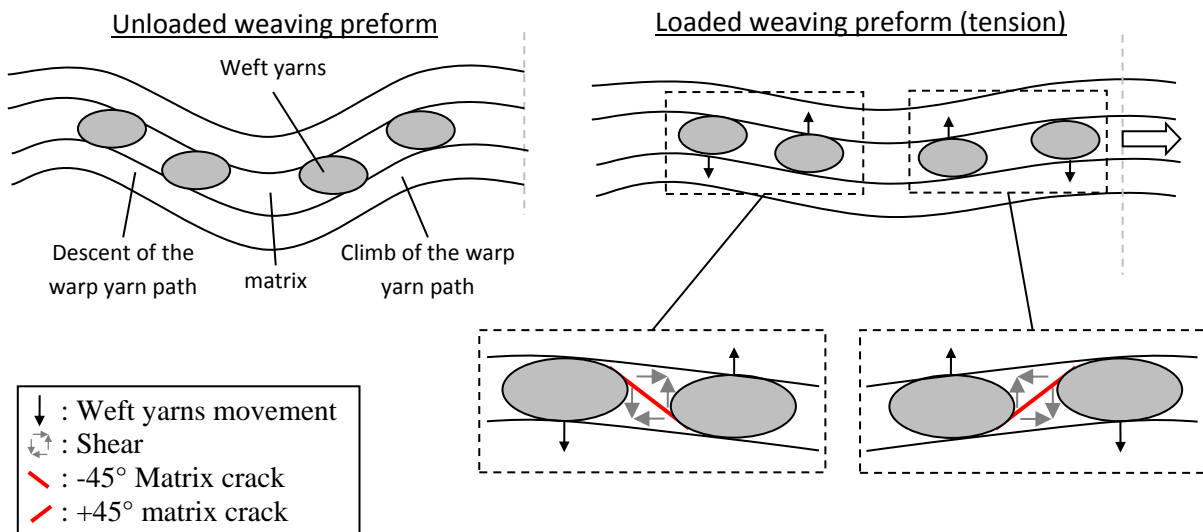


Figure 15 : Illustration of the weft yarns rearrangement and its consequences on shear strains and matrix cracks.

5.2. First damage envelope and associated mechanisms : plan $\sigma_{22} - \tau_{23}$

Second set of 4 bars, collected following the weft direction have allowed identifying first damage envelope in the stress plan ($\sigma_{22}-\tau_{23}$). Results issued from these several tests are illustrated in Figure 16. Damage mechanisms induced by specific loading conditions (torsion, proportional tensile-torsion and tensile loading) are also illustrated.

As seen on the figure, almost the same types of damage mechanisms as for the plan ($\sigma_{11}-\tau_{13}$) can be observed. It indicates that the same phenomena occur in this specific plan.

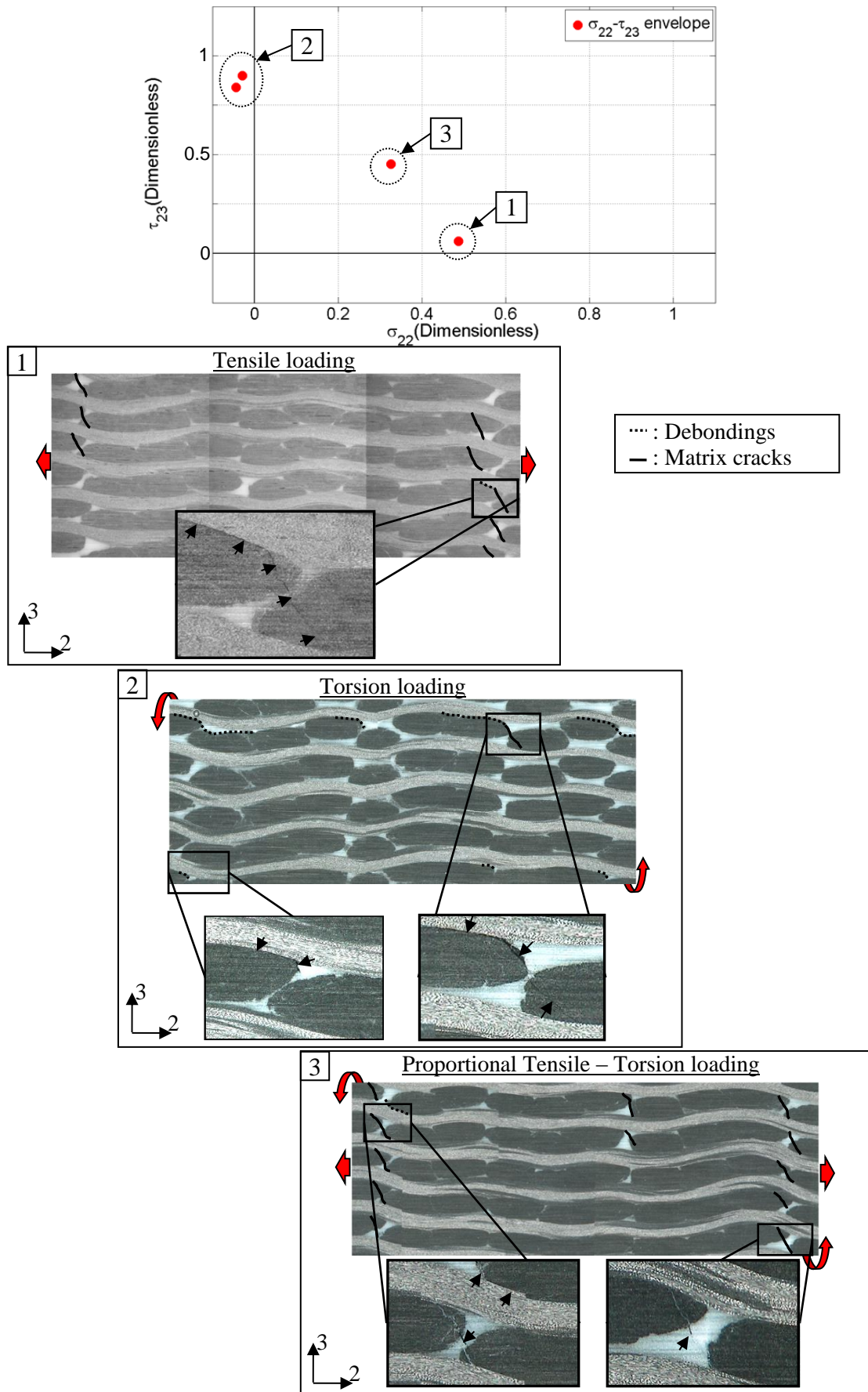


Figure 16 : First damage envelope on the σ_{22} - τ_{23} plan and illustration of the typical damage mechanisms observed under tensile (1), torsion (2) and proportional tensile-torsion (3) loadings.

6. Conclusion

In this study, the first damage envelope involving combined in-plane tensile and out-of-plane shear stress has been experimentally identified on a 3D woven composite with polymer matrix. To generate appropriate stress states in the material, proportional tensile-torsion loading have been applied to rectangular bars. To determine the first damage envelope, a robust methodology based on the use of several complementary investigation measurement techniques, including Stereo-DIC, Acoustic Emission acquisition and *in-situ* Video Microscopy, has been developed. By correlating results issued from these complementary investigation tools, onset of damage has been robustly identified. In addition, a specific data processing method, based on the work of Gong & al. [27], has been adapted to the case of proportional tensile-torsion tests to quantify accurately stress quantities encountered in such a composite material. Applying this methodology on an unbalanced 3D woven composite with polymer matrix, its first damage envelopes ($\sigma_{11}-\tau_{13}$) and ($\sigma_{22}-\tau_{23}$) have been successfully identified. Therefore, the validity of this experimental methodology has been demonstrated and its application can be extended to other in-plane damage envelopes such as ($\sigma_{11}-\tau_{12}$) and ($\sigma_{22}-\tau_{12}$) on composite materials having a complex woven structure.

From the strain fields measured by Stereo-DIC and the damage mechanisms observed by *in-situ* video-microscopy, several relations have been finally identified between the type of loading applied to the composite and its 3D woven architecture:

- The 3D woven architecture induces heterogeneous strain patterns, depending both on the 3D woven architecture and on the type of loading applied to the material.
- The strain patterns induced by multi-axial loading are nearly equal to the sum of the strains pattern induced by each of the uni-axial loadings.

- Multi-axial loading induces a combination of damage mechanisms resulting from individual damage mechanisms induced by each of the uni-axial loadings.

Experimental results of this study are currently used to identify multi-axial parameters of the macroscopic damage law Onera Damage Model (ODM) [14, 28].

7. Bibliography

- [1] A.P. Mouritz, M.K. Bannister, P.J. Falzon, and K.H. Leong, "Review of applications for advanced three-dimensional fibre textile composites", *Composites Part A: Applied science and manufacturing*, vol. 30, pp. 1445-1461, 1999.
- [2] J. Brandt, K. Dreschler, and F.-J. Arendts, "Mechanical performance of composites based on various three-dimensional woven-fibre preforms", *Composite science and technology*, vol. 56, no. 3, pp. 381-386, 1996.
- [3] M.N. Saleh, A. Yudhanto, P. Potluri, G. Lubineau, and C. Soutis, "Characterising the loading direction sensitivity of 3D woven composites: Effect of z-binder architecture", *Composites Part A: Applied Science and Manufacturing*, vol. 90, pp. 577-588, 2016.
- [4] B.N. Cox, M.S. Dadkhah, W.L. Morris, and J.G. Flintoff, "Failure mechanisms of 3D woven composites in tension, compression, and bending", *Acta Metallica Materialia*, vol. 42, no. 12, pp. 3967-3984, 1994.
- [5] P.J. Callus, A.P. Mouritz, M.K. Bannister, and K.H. Leong, "Tensile properties and failure mechanisms of 3D woven GRP composites", *Composite part A : Applied science and manufacturing*, vol. 30, pp. 1277-1287, 1999.
- [6] C. El Hage, R. Younes, Z. Aboura, M.L. Benzeggagh and M. Zoaeter, "Analytical and numerical modeling of mechanical properties of orthogonal 3D CFRP", *Composites Science and Technology*, Vol. 69, Issue 1, pp. 111-116, 2009.
- [7] A.E. Bogdanovich, M. Karahan, S.V. Lomov, and I. Verpoest, "Quasi-static tensile behavior and damage of carbon/epoxy composite reinforced with 3D non-crimp orthogonal woven fabric", *Mechanics of Materials*, vol. 62, pp. 14-31, 2013.
- [8] K.C. Warren, R.A. Lopez-Anido, and J. Goering, "Experimental investigation of three-dimensional woven composites", *Composite Part A : Applied science and manufacturing*, vol. 73, pp. 242-259, 2015.
- [9] J. Schneider, L. Marcin, Z. Aboura, and D. Marsal, "Experimental investigation and behavior modeling of a 3D Interlock woven fabric composite : Part 1", in *Proceedings of the 9th International Conference on Textile Composites - TEXCOMP9: Recent Advances in Textile*

Composites, pp.380-388, 2008.

- [10] P. Feissel, J. Schneider, Z. Aboura and P. Villon, "Use of diffuse approximation on DIC for early damage detection in 3D carbon/epoxy composites", *Composites Science and Technology*, vol. 88, pp. 16-25, 2013.
- [11] B. Yu, R.S. Bradley, C. Soutis, P.J. Hogg, and P.J. Withers, "2D and 3D imaging of fatigue failure mechanisms of 3D woven composites", *Composite Part A : Applied science and manufacturing*, vol. 77, pp. 37-49, 2015.
- [12] J. Henry, Z. Aboura, K. Khellil and S. Otin, "Suivi de l'endommagement en fatigue d'un composite à renfort Interlock Carbone/Epoxy par Emission Acoustique", in *Proceedings of the 17èmes Journées Nationales sur les Composites (JNC17)*, pp. 207, 2011.
- [13] B.K. Behera and B.P. Dash, "Mechanical behavior of 3D woven composites", *Materials and Design*, vol. 67, pp. 261–271, 2015.
- [14] A. Elias, F. Laurin, M. Kaminsky, and L. Gornet, "Experimental and numerical investigation of low energy/velocity impact damage generated in 3D woven composites with polymer matrix", *Composite structures*, no. 159, pp. pp. 228-239, 2017.
- [15] C. Davy and D. Marquis, "A multiaxial failure criterion for a brittle orthotropic composite", *Material and design*, vol. 24, pp. 15-24, 2003.
- [16] A.S. Chen and F.L. Matthews, "A review of multiaxial/biaxial loading tests for composite materials", *Composites*, vol. 24, no. 5, pp. 395-406, 1993.
- [17] M.S. Found, "Review of the multiaxial fatigue testing of fiber reinforced plastics", *Multiaxial Fatigue. ASTM STP 853*, pp. 381-395, January 1985.
- [18] S. Amijima, T. Fujii, and M. Hamaguchi, "Static and fatigue tests of a woven glass fabric composite under biaxial tension-torsion loading", *Composites*, vol. 22, no. 4, pp. 281-289, July 1991.
- [19] J. Navarro-Zafra, J.L. Curiel-Sosa, and M.C. Serna Moreno, "Mixed-mode damage into a CGRP cruciform subjected to biaxial loading", *Composite Structures*, vol. 133, pp. 1093-1100, 2015.
- [20] J.L.Y. Tan, V.S. Deshpande, and N.A. Fleck, "Failure mechanisms of a notched CFRP laminate under multi-axial loading", *Composites Part A: Applied Science and Manufacturing*, vol. 77, pp. 56-66, 2015.
- [21] T. Millot, "Study of an original 4 points bending-torsion loading test and application in behaviour modelisation of composites materials in complex state of stress", Doctorate thesis of Université de Besançon, 1990.
- [22] L. Ferry, D. Perreux, D. Varchona, and N. Sicot, "Fatigue behaviour of composite bars subjected

to bending and torsion", *Composites Science and Technology*, vol. 59, pp. 575-582, 1999.

- [23] S.G. Lekhnitskii, "*Theory of Elasticity of an Anisotropic Body*", Holden-Day Inc., Ed. San Francisco, 1963.
- [24] N. Tableau, Z. Aboura, K. Khellil, L. Marcin, and F. Bouillon, "Accurate measurement of in-plane and out-of-plane shear moduli on 3D woven SiC-SiBC material", *Composites Structures*, vol. 172, pp. 319-329, 2017.
- [25] K. Khellil, "Evaluation expérimentale d'un critère de rupture tensoriel polynomial tridimensionnel pour matériaux composites", Doctorate thesis of Université de Technologie de Compiègne, 1993.
- [26] S.S. Sonti, E.J. Barbero, and T. Winegardner, "Determination of Shear Properties for RP Pultruded Composites", *Journal of Reinforced Plastics and Composites*, vol. 14, no. 4, pp. 390-401, April 1995.
- [27] X.L. Gong, A. Laksimi, D.W. Lai, and M.L. Benzeggagh, "Stress Analysis in Unidirectional Composite Plates under Torque Loadings : Experimental Observation", *Journal of Reinforced Plastics and Composites*, 1995.
- [28] L. Marcin, "Modélisation du comportement, de l'endommagement et de la rupture de matériaux composites à renfort tissés pour le dimensionnement robuste des structures", Doctorate thesis of Université de Bordeaux 1, 2010.

8. Acknowledgements

The collaboration with Safran Aircraft Engines is gratefully acknowledged. This work was supported under the PRC Composites, French research project funded by DGAC, involving SAFRAN Group, ONERA and CNRS.